CFD-PBE coupled model for size-driven segregation in polydisperse granular flows

Monica Tirapelle[a], Andrea C. Santomaso[a], Luca Mazzei[b,*]

[a] *APTLab - Advanced Particle Technology Laboratory, Department of Industrial Engineering, University of Padova, Italy*
[b] *Department of Chemical Engineering, University College London, UK*

Abstract

Mixtures of granular materials made of different-sized particles may segregate when subjected to vibration or shear rate and in the presence of a gravitational field. This leads to highly inhomogeneous mixtures, which are undesirable in many industrial processes. This work focuses on size-driven segregation in polydisperse mixtures. We described the evolution of the particle size distribution through a Population Balance Equation (PBE), which we solved numerically with the Direct Quadrature Method of Moments. To allow segregation and micromixing to occur, we closed the size-conditioned velocity of the particles with a segregation-remixing model. The PBE was then included in an Eulerian-Eulerian model and solved in a commercial Computational Fluid Dynamics (CFD) code. We used the model to study granular flows down inclined planes. The numerical results were then compared with those obtained from Discrete Element Method simulations. The CFD-PBE model predicts well segregation and micromixing in packed beds of polydisperse powders.

Keywords: Size segregation, Population Balance Equation, Direct Quadrature Method of Moments, Polydispersity, CFD-PBE coupled model

*Corresponding author.
Email address : l.mazzei@ucl.ac.uk

1. Introduction

Granular materials consisting of particles with different properties may unexpectedly segregate when sheared in the presence of a gravitational field (Savage and Lun, 1988). Among the different properties, size is thought to be the most critical in driving segregation (Alonso et al., 1991). Two are the main mechanisms responsible for size-driven segregation: shear-induced particle percolation (or kinetic sieving) and squeeze expulsion (Savage and Lun, 1988). Their combination is referred to as gravity-driven segregation (Gray, 2018). The basic idea is that as the grains avalanche down-slope, the local void fraction fluctuates, and the small particles are more likely to percolate downwards through the gaps that create beneath them. Then, because of force imbalances, any-sized particle can be squeezed out of its own layer to an adjacent one. These two mechanisms result into a downward flux of small percolating particles and an upward flux of large rising particles (Bridgwater, 1994; Savage and Lun, 1988; Alonso et al., 1991).

In many practical situations, segregation is undesirable; for instance, it can reduce the performance of a packed bed and degrade the quality and safety of a solid product. Furthermore, segregation-related issues increase production costs and wastes of many pharmaceutical, chemical and agricultural processes (Bridgwater, 1976; Standish, 1985; Ottino and Khakhar, 2000; Gray and Ancey, 2011).

Even if segregation has been studied for nearly a century, and a lot of efforts have been made to understand its underlying physical mechanisms (Fan et al.,

2017; Umbanhowar et al., 2019; Volpato et al., 2020), a quantitative analysis of the phenomenon is still lacking, and much remains to be done (Alonso et al., 1991; Ottino and Khakhar, 2000; McCarthy, 2009). Design decisions are still made without a fundamental understanding of the phenomenon and, to minimize the effects of segregation, process engineers still rely on empirical heuristic rules and avoidance practices (Ottino and Khakhar, 2000; McCarthy, 2009). One of the most important limitations, which is present also in many advanced studies, is that mixtures are assumed to be binary or ternary. But real mixtures are polydisperse, in particular over their size (Mazzei, 2013; Strumendo and Arastoopour, 2008).

Here, we focus on cohesionless powders characterized by a particle size distribution. To account for particle polydispersity and describe the evolution in time and space of the particle size distribution, we used the Population Balance Equation (PBE) (Arastoopour et al., 2017). Although in theory PBEs can be solved analytically, only few analytical solution strategies have been developed. Therefore, population balance equations are usually solved numerically. Many numerical methods are available, such as the method of Laplace transforms, the method of moments, the method of weighted residuals and the Monte Carlo method (Ramkrishna, 2000; Arastoopour et al., 2017). The Method of Moments, or MOM, is computationally attractive because provides good results at low computational cost (Arastoopour et al., 2017). It consists in tracking the lower-order moments of the distribution function with transport equations. In its classical form, the MOM requires that the functional form of the distribution

function remain the same during the process. Furthermore, a moment closure problem arises because, for any given set of moments the modeller wishes to track, higher-order moments feature in the transport equations (Marchisio and Fox, 2007; Mazzei, 2011). In the Quadrature Method of Moments (QMOM), the closure problem is overcome via a quadrature-based approximation of the particle size distribution. This formulation of the MOM was first developed by McGraw (1997) for modelling the evolution of aerosols, and then further developed by Marchisio and co-workers for modelling crystal growth, aggregation and breakage (Marchisio et al., 2003a,b). In this approach, a few drawbacks still exist: the reconstruction of the distribution function from a finite set of moments is impossible, unless one knows a-priori the functional form of the Particle Size Distribution (PSD), and the computational cost is higher than in MOM since weights and nodes have to be back-calculated from the moments of the distribution at each time step in each cell of the computational domain (Strumendo and Arastoopour, 2008; Mazzei et al., 2012; Arastoopour et al., 2017). Furthermore, when a number of moments greater than four is tracked, the higher-order moments corrupt leading to non-physical values of quadrature nodes (Mazzei et al., 2012). To overcome the disadvantages of QMOM, Marchisio and Fox (2005) proposed the Direct Quadrature Method of Moments (DQMOM). This differs from the QMOM because it tracks directly the weights and nodes of the quadrature approximation rather than tracking the moments of the PSD (Arastoopour et al., 2017). Since both methods adopt the same approximation of the PSD, they are theoretically equivalent (Mazzei, 2013). The Finite size domain

Complete set of trial functions Method Of Moments (FCMOM) by Strumendo and Arastoopour (2008) is another promising formulation, since it does not require specific assumptions for the distribution function and it converges fast to the solution of the PBE. It differs from the other approaches because it still solves the PBE in terms of its lower moments, but then reconstructs the distribution function itself (Arastoopour et al., 2017). However, since the FCMOM assumes that all particles, independently of their internal properties (e.g. size), are convected with an average phase velocity, it cannot be applied to model size-driven segregation.

In this work, we implemented the version of DQMOM developed by Mazzei et al. (2010), in which the average phase velocity is replaced with a size-conditioned velocity. To determine the size-conditioned velocities, Mazzei et al. (2010) used the averaged dynamical equations of multiphase flows, whereas we closed them constitutively using a segregation-remixing model. The transport equations obtained from the DQMOM were then integrated within an Eulerian-Eulerian framework and solved in a Computational Fluid Dynamics (CFD) software.

We applied this coupled CFD-PBE model to simulate the segregation dynamics of an inert, dry and cohesionless polydisperse powder, initially uniformly mixed, flowing down an inclined plane. We chose to simulate a chute flow because of its relative simplicity, which allows developing and testing new theories (Bhattacharya and McCarthy, 2014). To test the accuracy of the model, we compared its results to those of a Discrete Element Method (DEM) model.

Even if the CFD-PBE model appears to be complex, it predicts well the evolution in time and space of the particle size distribution for a wide range of bed depths. Its main advantage with respect to DEM is that the computation time required is lower.

The paper is organized as follows. In Section 2, we introduce the PBE, we discuss the closure for the size-conditioned particle velocity and we describe the DQMOM, i.e. the solution technique we employed. Section 3 deals with the CFD-PBE coupling and with the closure of the effective stress tensor of the mixture. The CFD implementation in Ansys Fluent is described in Sections 4, while in Section 5, we present the DEM framework used to validate the model. In Section 6, the results are reported and compared with DEM findings. Conclusions are drawn in Section 7.

2. The population balance equation and solution methods

The evolution of a polydisperse solid phase can be mathematically described at the mesoscopic level by the Generalized Population Balance Equation (GPBE) (Marchisio and Fox, 2007). Starting from this equation, in this section we derive the DQMOM transport equations. Firstly, we express the GPBE in terms of Volume Density Function (VDF). Then, in order to solve the PBE within the CFD code and determine the VDF, we reduce to one the dimensionality of the internal state space of the PBE (Section 2.1) and we approximate the VDF with a quadrature formula (Section 2.3). The reduced PBE features an unclosed term: the size-conditioned velocity. As closure relation, we use a segregation-remixing

model from the literature (Section 2.2). The problem reduces to solving $2n$ transport equations for quadrature weights and weighted nodes where n is the number of classes in the quadrature approximation.

2.1. The Generalized PBE

Let us consider a particle population characterized by two internal coordinates: the particle size ξ (scalar quantity) and the particle velocity $\boldsymbol{v}$ (vector quantity). The equation that includes also the particle velocity vector as internal mesoscale variable is referred to as generalized population balance equation (Marchisio and Fox, 2013). To describe the population of particles, we used a volume density function (VDF) $f_v(\boldsymbol{v}, \xi; \boldsymbol{x}, t)$ that represents the volume of particles with size ξ in the range $\mathrm{d}\xi$ and velocity $\boldsymbol{v}$ in the range $\mathrm{d}\boldsymbol{v}$ that are, at time t, contained in the volume $\mathrm{d}\boldsymbol{x}$ around $\boldsymbol{x}$. If neither reactions nor attrition occur, the GPBE expressed in terms of volume density function reads (Mazzei et al., 2010):

$$\begin{gathered} \frac{\partial}{\partial t} f_v(\boldsymbol{v}, \xi; \boldsymbol{x}, t) + \nabla_x \cdot [f_v(\boldsymbol{v}, \xi; \boldsymbol{x}, t)\, \boldsymbol{v}] + \\ \nabla_{\boldsymbol{v}} \cdot [f_v(\boldsymbol{v}, \xi; \boldsymbol{x}, t)\, \boldsymbol{A}_p(\boldsymbol{v}, \xi; \boldsymbol{x}, t)] = S_v(\boldsymbol{v}, \xi; \boldsymbol{x}, t) \end{gathered} \tag{1}$$

where $\boldsymbol{x}$ is the position vector in real space, $\boldsymbol{A}_p$ is the continuous rate of change of particle velocity (i.e. the velocity of the particles in the velocity subspace) and S_v is the source term that accounts for discontinuous jumps both in the velocity state space due to particle collisions and in the size space caused by aggregation and breakage. Note that in the GPBE diffusion in physical space is never present.

Eq. 1 governs the spatial and temporal evolution of the VDF. Solving it is extremely difficult: it is an integro-differential equation with respect to the internal variables, and its dimensionality is higher than the classical transport equations (it is four dimensional in its internal state space) (Mazzei et al., 2010; Strumendo and Arastoopour, 2008; Arastoopour et al., 2017). To reduce the dimensionality of the internal state space, we integrate out the coordinate $\boldsymbol{v}$, so that Eq. 1 reduces to:

$$\frac{\partial}{\partial t}\hat{f}_v\left(\xi;\boldsymbol{x},t\right)+\nabla_x\cdot\left[\hat{f}_v\left(\xi;\boldsymbol{x},t\right)\tilde{\boldsymbol{v}}(\xi;\boldsymbol{x},t)\right]=0 \tag{2}$$

where, by definition, it is:

$$\hat{f}_v\left(\xi;\boldsymbol{x},t\right)\equiv\int_{\Omega_v} f_v\left(\boldsymbol{v},\xi;\boldsymbol{x},t\right)\mathrm{d}\boldsymbol{v} \tag{3}$$

$$\hat{f}_v\left(\xi;\boldsymbol{x},t\right)\tilde{\boldsymbol{v}}(\xi;\boldsymbol{x},t)\equiv\int_{\Omega_v} f_v\left(\boldsymbol{v},\xi;\boldsymbol{x},t\right)\boldsymbol{v}\mathrm{d}\boldsymbol{v} \tag{4}$$

with $\Omega_v\equiv\mathbb{R}$ denoting the domain of variation of $\boldsymbol{v}$. In the reduced PBE (Eq. 2), since the particle velocity is no longer an internal coordinate, the source term vanishes because no discontinuous jumps take place in the size space (i.e. particles neither aggregate or break) and $\hat{f}_v\left(\xi;\boldsymbol{x},t\right)$ is a monovariate VDF with particle size being its only internal state variable. There is, however, an unclosed term: the mean velocity conditioned on the particle size $\tilde{\boldsymbol{v}}(\xi;\boldsymbol{x},t)$. To close $\tilde{\boldsymbol{v}}$ one must either solve a balance equation, as done by Mazzei et al. (2010), or use a constitutive relation. In this work, we employed a constitutive relation.

2.2. Size-conditioned velocity

In dense, gravity-driven, free-surface flows of granular avalanches with dissimilar grains, segregation takes place. Two are the competitive mechanisms characterising segregation: gravity-driven size segregation and diffusive remixing caused by the random motion of the particles as they collide and shear over one another (Bridgwater, 1976; Savage and Lun, 1988; Gray and Chugunov, 2006). Gravity-driven size segregation is the combination of kinetic sieving and squeeze expulsion; it results in a net segregating flux of the smaller particles downwards and of the larger particles upwards (Savage and Lun, 1988). Competing against segregation, there is diffusive remixing (Gray and Chugunov, 2006). To account for remixing, one includes a diffusional term in the model, and therefore an associated diffusion coefficient $\mathscr{D}$. Unfortunately, there is no theory on diffusion that applies to dense polydisperse granular flows, so here we assumed that diffusion is isotropic and that $\mathscr{D}$ is a constant (i.e. it does not even depend on the particle size). Particles are then conveyed by the main solid flow, whose velocity (i.e. the Eulerian velocity of the mixture) is governed by the dynamical equation of the mixture.

In light of these considerations, three terms contribute to the mass flux of the particles in a gravity-driven size segregating system: 1) a segregative flux caused by kinetic sieving and squeeze expulsion, 2) a diffusive flux responsible for remixing and 3) an advective flux that conveys particles down-slope. We

can thus write:

$$\hat{f}_v(\xi;\boldsymbol{x},t)\tilde{\boldsymbol{v}}(\xi;\boldsymbol{x},t) = \hat{f}_v(\xi;\boldsymbol{x},t)\boldsymbol{v}_b(\boldsymbol{x},t) + \hat{f}_v(\xi;\boldsymbol{x},t)\boldsymbol{v}_s(\xi;\boldsymbol{x},t) - \mathscr{D}\nabla_x\hat{f}_v\left(\xi;\boldsymbol{x},t\right) \tag{5}$$

where $\boldsymbol{v}_b(\boldsymbol{x},t)$ is the Eulerian velocity of the solid mixture and $\boldsymbol{v}_s(\xi;\boldsymbol{x},t)$ is the size-dependent segregation velocity.

If we consider a chute flow, the coordinate system has the x-, y- and z-axis in the stream-wise, span-wise and surface normal direction, respectively. Thus, the y-component of the segregation velocity is much smaller than the other two components (i.e. $v_{s,y} \approx 0$) and the segregation velocity in Cartesian index notation reads:

$$\boldsymbol{v}_s(\xi;\boldsymbol{x},t) = v_{s,x}(\xi;\boldsymbol{x},t)\boldsymbol{e}_x + v_{s,z}(\xi;\boldsymbol{x},t)\boldsymbol{e}_z \tag{6}$$

To model the x- and z-components of the segregation velocity, different segregation laws can be employed, since a general and valid description of the continuum segregation model is still lacking. In this study, we arbitrarily chose the expression proposed by Marks et al. (2012):

$$v_{s,x}(\xi;\boldsymbol{x},t) = \dot{\gamma}\left(\frac{g\cdot\sin\theta}{c}\right)(f_c - 1) \tag{7}$$

$$v_{s,z}(\xi;\boldsymbol{x},t) = \dot{\gamma}\left(\frac{g\cdot\cos\theta}{c}\right)(f_c - 1) \tag{8}$$

where g is the acceleration due to gravity, θ is the angle of inclination with respect to the horizon, $\dot{\gamma}$ is the shear rate, and c is a coefficient of inter-particle drag with unit of $1/\mathrm{s}^{-2}$. $\dot{\gamma}$ is proportional to the magnitude of the deviatoric

part of the strain-rate tensor $\boldsymbol{S}$:

$$\dot{\gamma} = 2||\boldsymbol{S}|| \tag{9}$$

where $||\boldsymbol{S}|| \equiv \sqrt{\mathrm{tr}(\boldsymbol{S}^2)/2}$ is the second invariant of the tensor S. About c, its nature is still poorly understood, so we assume it to be a constant. We also assume that the scaling factor for the multicomponent case, f_c, scales with the characteristic length of the particle, ξ (Marks et al., 2012; Tunuguntla et al., 2014):

$$f_c = \frac{\xi}{\int_0^\infty \hat{f}_v(\xi;\boldsymbol{x},t)\xi \,\mathrm{d}\xi} \tag{10}$$

Note that one could employ other forms for the percolation velocity. Introducing Eq. 5 in the reduced population balance equation (Eq. 2) gives:

$$\frac{\partial}{\partial t}\hat{f}_v + \nabla_x \cdot \left(\hat{f}_v \boldsymbol{v}_b\right) + \nabla_x \cdot \left(\hat{f}_v \boldsymbol{v}_s\right) - \mathscr{D}\nabla_x^2 \hat{f}_v = 0 \tag{11}$$

This equation governs the evolution of the monovariate VDF $\hat{f}_v\left(\xi;\boldsymbol{x},t\right)$. The model relies on two parameters, the drag coefficient and the diffusivity. We will see in Section 2.3 that, because of the inclusion of diffusion, a source term will appear in the DQMOM transport equation.

2.3. Direct Quadrature Method of Moments

There are many solution methods for population balance equations. However, for practical needs, knowing the evolution of the first few moments of the VDF is enough to fulfil engineering requirements (Ramkrishna, 2000). The idea behind the method of moments is solving the density function in terms of its lower-order moments by integrating out the size coordinate from the PBE

(Mazzei et al., 2010; Arastoopour et al., 2017). However, this method involves a closure problem: for any given set of moments, the equations involve higher-order moments external to the set. This makes the MOM rarely applicable. The quadrature method of moments presented by McGraw (1997) eliminates the closure problem by approximating the VDF with quadrature formulas.

In this work, we solved the population balance equation with the direct quadrature method of moments. The volume density function $\hat{f}_v$ in Eq. 11 is approximated as a summation of n Dirac delta functions:

$$\hat{f}_v \approx \sum_{\alpha=1}^{n} \phi_\alpha(\boldsymbol{x}, t)\delta\left(\xi - \xi_\alpha(\boldsymbol{x}, t)\right) \tag{12}$$

where n is the number of classes of the quadrature approximation, while ϕ_α and ξ_α are the weights and nodes of the α-th quadrature class, respectively.

We assume that the void fraction in the granular mixture ε is constant, uniform and equal to 0.37. Thus, the overall solid volume fraction is always equal to $(1-\varepsilon) = 0.63$. Because of this assumption, we could work in terms of void-free VDF (i.e. its weights sum to one), and so void-free quadrature weights in the quadrature formula. From now on, we refer to $\hat{f}_v$ as void-free VDF.

Introducing Eq. 12 in Eq. 11 gives:

$$\begin{aligned} &\frac{\partial}{\partial t}\left(\sum_{\alpha=1}^{n} \phi_\alpha \delta\left(\xi - \xi_\alpha\right)\right) + \nabla_x \cdot \left(\sum_{\alpha=1}^{n} \phi_\alpha \delta\left(\xi - \xi_\alpha\right) \boldsymbol{v}_b\right) + \\ &\nabla_x \cdot \left(\sum_{\alpha=1}^{n} \phi_\alpha \delta\left(\xi - \xi_\alpha\right) \boldsymbol{v}_{s,\alpha}\right) - \mathscr{D}\nabla_x^2 \left(\sum_{\alpha=1}^{n} \phi_\alpha \delta\left(\xi - \xi_\alpha\right)\right) = 0 \end{aligned} \tag{13}$$

where $\boldsymbol{v}_{s,\alpha}(\boldsymbol{x}, t)$ is the segregation velocity of the particles belonging to the quadrature class α. Since both $\phi_\alpha(\boldsymbol{x}, t)$ and $\xi_\alpha(\boldsymbol{x}, t)$ are functions of the real

space coordinates and the time, Eq. 13 yields:

$$\sum_{\alpha=1}^{n}\left[c_{\alpha}^{\phi}(\boldsymbol{x},t)\delta\left(\xi-\xi_{\alpha}\right)-(c_{\alpha}^{\phi\xi}(\boldsymbol{x},t)-\xi_{\alpha}c_{\alpha}^{\phi}(\boldsymbol{x},t))\delta'\left(\xi-\xi_{\alpha}\right)\right]= \sum_{\alpha=1}^{n}\left[\mathscr{D}\delta''\phi_{\alpha}\nabla_{x}\xi_{\alpha}\cdot\nabla_{x}\xi_{\alpha}\right] \tag{14}$$

where we defined:

$$\frac{\partial}{\partial t}\phi_{\alpha}+\nabla_{x}\cdot(\phi_{\alpha}\boldsymbol{v}_{b})+\nabla_{x}\cdot(\phi_{\alpha}\boldsymbol{v}_{s,\alpha})-\mathscr{D}\nabla_{x}^{2}\phi_{\alpha}\equiv c_{\alpha}^{\phi} \tag{15}$$

$$\frac{\partial}{\partial t}\sigma_{\alpha}+\nabla_{x}\cdot(\sigma_{\alpha}\boldsymbol{v}_{b})+\nabla_{x}\cdot(\sigma_{\alpha}\boldsymbol{v}_{s,\alpha})-\mathscr{D}\nabla_{x}^{2}\sigma_{\alpha}\equiv c_{\alpha}^{\sigma} \tag{16}$$

with $\sigma_{\alpha}\equiv(\phi_{\alpha}\xi_{\alpha})$ being the α-*th* weighted node.

Equation 14 expresses the population balance equation for a monovariate population of particles whose size-conditioned velocity is closed as reported in Section 2.2. The unknowns functions are $\phi_{\alpha}(\boldsymbol{x},t)$ and $\xi_{\alpha}(\boldsymbol{x},t)$, namely the weights and the nodes of the quadrature approximation. Also, the source terms $c_{\alpha}^{\phi}(\boldsymbol{x},t)$ and $c_{\alpha}^{\phi\xi}(\boldsymbol{x},t)$ are unknowns, but they can be determined by computing the moment transforms of the PBE, namely by forcing the quadrature-based VDF to agree with the first $2n$ integer moments of the actual VDF (Mazzei, 2011). By definition, the *k-th* order integer moment of $\hat{f}_{v}$, with $\hat{f}_{v}$ approximated as reported in Eq. 12, reads:

$$\mathscr{M}_{k}\equiv\int_{0}^{\infty}\xi^{k}\hat{f}_{v}\left(\xi;\boldsymbol{x},t\right)\mathrm{d}\xi\approx\sum_{\alpha=1}^{n}\phi_{\alpha}(\boldsymbol{x},t)\xi_{\alpha}^{k}(\boldsymbol{x},t) \tag{17}$$

If we apply this transform to each term of Eq. 14, we obtain a linear algebraic

system in the $2n$ unknown source terms c_α^ϕ and $c_\alpha^{\phi\xi}$:

$$\begin{aligned} \sum_{\alpha=1}^{n} c_\alpha^\phi \xi_\alpha^k + k \sum_{\alpha=1}^{n} (c_\alpha^{\phi\xi} - \xi_\alpha c_\alpha^\phi) \xi_\alpha^{k-1} = \\ k(k-1) \sum_{\alpha=1}^{n} \mathscr{D} \phi_\alpha \xi_\alpha^{k-2} \nabla_x \xi_\alpha \cdot \nabla_x \xi_\alpha \,, \; k \in [0, 2n-1] \end{aligned} \tag{18}$$

In this work, we employed a two-node quadrature approximation; thus we obtained four source terms:

$$\begin{cases} c_1^\phi(\boldsymbol{x}, t) = -6(\chi_1 - \chi_2)(\xi_1 - \xi_2)^{-2} \\ c_1^{\phi\xi}(\boldsymbol{x}, t) = [2\chi_2(2\xi_1 + \xi_2) - 2\chi_1(\xi_1 + 2\xi_2)](\xi_1 - \xi_2)^{-2} \\ c_2^\phi(\boldsymbol{x}, t) = -c_1^\phi(\boldsymbol{x}, t) \\ c_2^{\phi\xi}(\boldsymbol{x}, t) = -c_1^{\phi\xi}(\boldsymbol{x}, t) \end{cases} \tag{19}$$

where the subscript 1 or 2 indicates the quadrature class, and χ_α is equal to:

$$\chi_\alpha \equiv \mathscr{D} \phi_\alpha \nabla_x \xi_\alpha \cdot \nabla_x \xi_\alpha \tag{20}$$

Now that the source terms are known, solving the PBE reduces to solving Eqs. 15 and 16 for each quadrature class. If one wanted to track directly the evolution in time and space of the quadrature nodes instead of the weighted nodes, the transport equation would be:

$$\frac{\partial}{\partial t} \xi_\alpha + \boldsymbol{v}_b \cdot \nabla_x \xi_\alpha + \boldsymbol{v}_{s,\alpha} \cdot \nabla_x \xi_\alpha - \mathscr{D} \nabla_x^2 \xi_\alpha = c_\alpha^\xi \tag{21}$$

with the source term equal to:

$$c_\alpha^\xi \equiv \frac{c_\alpha^\sigma - c_\alpha^\phi \xi_\alpha + 2\mathscr{D} \nabla_x \phi_\alpha \cdot \nabla_x \xi_\alpha}{\phi_\alpha} \tag{22}$$

As explained in Mazzei (2011), the diffusive terms generate the source terms. In our case, spatial diffusion arises in the transport equations because $\boldsymbol{v}_\alpha$ has

been closed using the segregation-remixing model, which is made of two competitive mechanisms: gravity-driven segregation and diffusive remixing. Thus, since we have diffusion, we also have generation. Furthermore, diffusion consents micromixing: each element can interact with the other elements within the domain so that powders are allowed to mix also at the microscopic length scale (Mazzei et al., 2010; Mazzei, 2011).

3. Multiphase fluid dynamic model

3.1. CFD-PBE coupling

Process operations such as storage, conveying, mixing and sizing of particles range from small scale (e.g. pharmaceutical industries) to large scale (e.g. minerals industries). Simulating large-scale systems via DEM may be unfeasible because of the required computational effort and time. However, to cope with a full-scale industrial system, one can use computational fluid dynamic simulations. For this reason, we developed a segregation CFD-PBE coupled model to be implemented in a CFD code. The flowchart of the CFD-PBE coupled model is reported in Fig. 1. We simulated a two-phase system consisting of two phases: the granular mixture flowing down an inclined plane, and the air lying above the mixture. We used the VOF modelling approach, which allows calculating the velocity and volume fraction profiles in the two phases. The volume fraction is uniform in the bulk of each phase, varying only near the interface between the two phases. The velocity field in the granular phase coincides with $\boldsymbol{v}_b$, the bulk velocity featuring in the PBE (see Eq. 11). Once the segregation fluxes

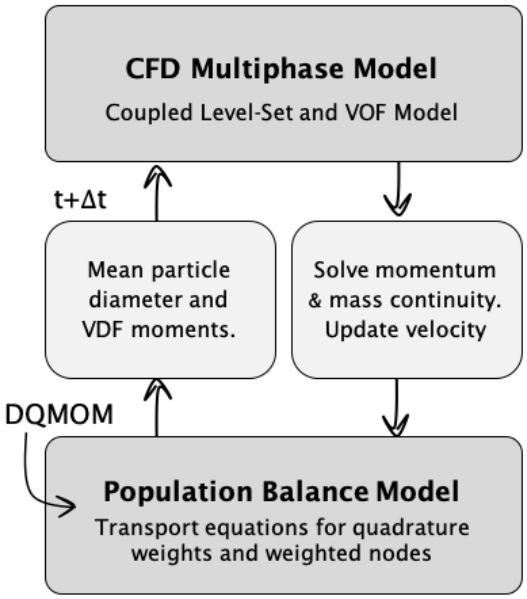

Figure 1: Schematic diagram of the CFD-PBE coupled model. The PBE is solved by adopting the DQMOM.

are obtained, the PBE is solved by adopting the DQMOM. Since segregation determines changes in the local rheology, and consequently the flow, the nodes and weights of the quadrature approximations are then fed back into the CFD model and used to update the local rheology of the bulk solid at the subsequent time step.

3.2. Multifluid dynamical equations

We considered a polydisperse powder flowing down an inclined plane under gravity and in ambient conditions. We limited our investigation to a two-dimensional incompressible granular flow. As already mentioned, we assumed

that the mean solid volume fraction $1 - \varepsilon$ is constant within the powder bed (Gray and Thornton, 2005). Because of these assumptions, the polydisperse granular material can be represented as a single continuous phase. The second phase is instead superficial ambient air. The two phases do not interpenetrate, and mass transfer does not occur.

As Eulerian-Eulerian multiphase model, we employed the coupled level-set and volume of fluid (VOF) method, a numerical technique designed for immiscible fluids that allows tracking the position of the interface. In the VOF method, pressure and velocity field $\boldsymbol{u}$ are found by solving the mass and momentum equations:

$$\frac{\partial \rho}{\partial t} + \nabla \cdot (\rho \boldsymbol{u}) = 0 \tag{23}$$

$$\frac{\partial}{\partial t}(\rho \boldsymbol{u}) + \nabla \cdot (\rho \boldsymbol{u}\boldsymbol{u}) = \nabla \cdot \boldsymbol{\sigma} + \rho \boldsymbol{g} \tag{24}$$

where $\boldsymbol{\sigma}$ is the effective stress tensor. The closure of the effective stress tensor is discussed in Section 3.3. The material properties required in Eq. 24 are determined by the presence of the component phase in each control volume. In a two phase system, density and viscosity are respectively:

$$\rho = (1 - \alpha_s)\rho_{air} + \alpha_s \rho_s \tag{25}$$

$$\eta = (1 - \alpha_s)\eta_{air} + \alpha_s \eta_s \tag{26}$$

where α_s is the volume fraction of solid. In this way, the discontinuity across the interface is smooth, whereas away from the interface air and solid maintain their

characteristic properties (Olsson et al., 2007; Dianat et al., 2017). The volume fraction of the solid phase is obtained by solving the transport equation:

$$\frac{\partial \alpha_s}{\partial t} + \nabla \cdot (\alpha_s \boldsymbol{u}) = 0 \tag{27}$$

whereas, the volume fraction of air is computed based on the following constraint:

$$\alpha_{air} = 1 - \alpha_s \tag{28}$$

The interface between air and solid is captured by the level-set method. The level-set $\psi(\boldsymbol{x}, t)$ is a continuous function defined as the signed distance from the interface. In a two-phase flow system, the level-set is zero at the interface, positive in the primary phase (i.e. air) and negative in the secondary phase (i.e. solid) (Dianat et al., 2017):

$$\psi(\boldsymbol{x}, t) \begin{cases} +|\delta| & \boldsymbol{x} \in \text{ primary phase} \\ 0 & \text{at the interface} \\ -|\delta| & \boldsymbol{x} \in \text{ secondary phase} \end{cases} \tag{29}$$

where δ denotes the distance from the interface. The level-set advection equation is:

$$\frac{\mathrm{D}\psi}{\mathrm{D}t} = 0 \tag{30}$$

As mentioned, in the solid phase the velocity $\boldsymbol{u}$ coincides with the velocity $\boldsymbol{v_b}$ featuring in Eq. 11.

3.3. Effective stress tensor

The stress tensor $\boldsymbol{\sigma}$ in Eq. 24 can be decomposed into an isotropic and a deviatoric part:

$$\boldsymbol{\sigma} = -p\boldsymbol{I} + \boldsymbol{\tau} \tag{31}$$

where p is the pressure (i.e. it derives from the mass conservation in Eq. 23), $\boldsymbol{I}$ is the identity tensor and $\boldsymbol{\tau}$ is the deviatoric stress tensor. Closing $\boldsymbol{\sigma}$ therefore reduces to expressing constitutively $\boldsymbol{\tau}$. The closure of $\boldsymbol{\tau}$ is achieved by specifying three constitutive equations: a flow rule, an alignment condition and a plastic yield condition (Barker and Gray, 2017). Let us beginning with the flow rule. If we consider incompressible granular systems, the flow rule far from the interface between solid and air is:

$$\nabla \cdot \boldsymbol{u} = 0 \tag{32}$$

The alignment condition is formulated in terms of the strain rate tensor, $\boldsymbol{D}$ (Barker and Gray, 2017; Heyman et al., 2017; Schaeffer et al., 2019):

$$\boldsymbol{D} \equiv \frac{1}{2}\left(\nabla \cdot \boldsymbol{u} + \nabla \cdot \boldsymbol{u}^T\right) \tag{33}$$

and reads:

$$\frac{\boldsymbol{\tau}}{||\boldsymbol{\tau}||} = \frac{\boldsymbol{D}}{||\boldsymbol{D}||} \tag{34}$$

where $||\cdot||$ denotes the second invariant. This conditions states that the principal directions (i.e. eigenvectors) of $\boldsymbol{\tau}$ and $\boldsymbol{D}$ must be aligned (i.e. parallel) (Pitman and Schaeffer, 1987). The third constitutive equation, take the form of a generalized yield condition that relates $||\boldsymbol{\tau}||$ with the pressure:

$$||\boldsymbol{\tau}|| = \mu p \tag{35}$$

being μ the effective friction coefficient. Introducing the yield condition (Eq. 35) into the alignment condition (Eq. 34) leads to a closure relation for the deviatoric stress tensor:

$$\boldsymbol{\tau} = \mu p \frac{\boldsymbol{D}}{||\boldsymbol{D}||} \tag{36}$$

If we consider that for incompressible granular flows $\dot{\gamma} = 2||\boldsymbol{D}||$, and if we substitute the definition of $\boldsymbol{D}$ (Eq. 33), Eq. 36 becomes:

$$\boldsymbol{\tau} = \frac{\mu p}{\dot{\gamma}} \left(\nabla \cdot \boldsymbol{u} + \nabla \cdot \boldsymbol{u}^T \right) \tag{37}$$

Thus, the closure of $\boldsymbol{\tau}$ is achieved by customizing the frictional viscosity of the solid phase:

$$\eta_s = \frac{\mu p}{\dot{\gamma}} \tag{38}$$

In Ansys Fluent, this can be done by means of customized user define functions. In Eq. 38 there is still an unknown: the effective friction coefficient μ. To close it, we used the incompressible $\mu(I)-$ rheology proposed by the Groupement De Recherche Milieux Divisés (G. D. R. MiDi, 2004). The incompressible $\mu(I)$ rheology (G. D. R. MiDi, 2004; Jop et al., 2006) states that the friction coefficient μ is rate dependent and scales with the inertial number I. For mono-sized particulate flows, the inertial number takes the form (G. D. R. MiDi, 2004; Da Cruz et al., 2005):

$$I = \frac{d\dot{\gamma}}{\sqrt{p/\rho_s^*}} \tag{39}$$

where d is the particle diameter and ρ_s^* is the intrinsic solid density. Note that ρ_s^*, which is defined as the mass of the solid per unit constituent volume, differs from the bulk density $\rho_s \equiv (1-\varepsilon) \cdot \rho_s^*$, which is instead associated with the

total volume the solid occupies. The most frequently used form for expressing the local frictional coefficient as a function of I has been proposed by Jop et al. (2006):

$$\mu(I) = \mu_s + \frac{\mu_2 - \mu_s}{I_0/I + 1} \tag{40}$$

In the friction law, μ_s is the static friction coefficient, μ_2 is the limiting value toward which the friction coefficient converges at high inertial number, and I_0 is a constant. The friction coefficient expressed in this way is an increasing monotonic function: it starts from the critical minimum value μ_s for zero shear and increases asymptotically to μ_2 when I diverges.

Since the dependence of the rheology on the particle size distribution is still matter of research (Yohannes and Hill, 2010; Marks et al., 2012), we assumed that the friction law in Eq. 40 holds also for polydisperse granular materials, with:

$$I = \frac{\mathcal{D}\dot{\gamma}}{\sqrt{p/\rho_s^*}} \tag{41}$$

where $\mathcal{D}$ is the average diameter of the PSD (Tripathi and Khakhar, 2011; Rognon et al., 2007), expressed as the ratio between the first and the zeroth moments of the distribution:

$$\mathcal{D} = \frac{\sum_k \phi_\alpha \xi_\alpha}{\sum_k \phi_\alpha} = \frac{\mathcal{M}_1}{\mathcal{M}_0} \tag{42}$$

To sum up, the closure of $\boldsymbol{\tau}$ is achieved by introducing a user defined function for the frictional viscosity of the solid (Eq. 38), where μ is function of a generalized Inertial number definition (Eq. 41). This is the simplest hypothesis we could employ for polydisperse mixtures.

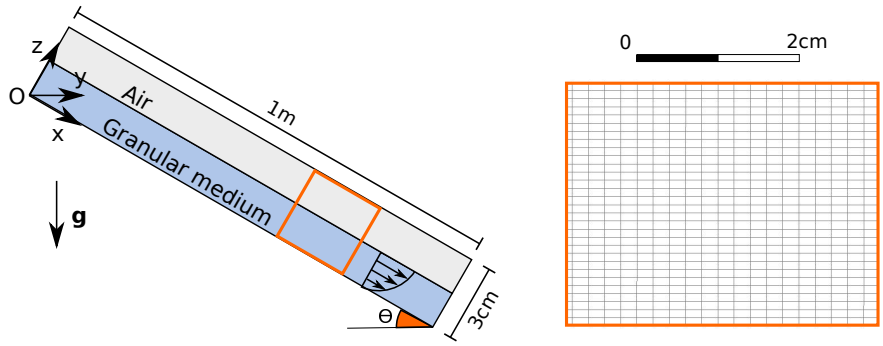

Figure 2: On the left: a sketch of the simulated system and the coordinate system. The blue shaded area represents the solid phase and θ is the inclination angle of the chute. On the right: a piece of the 2D mesh employed in the CFD simulation.

4. CFD implementation

The CFD-PBE coupled model was implemented in a CFD code to predict the evolution of the PSD of a polydisperse system flowing down an inclined plane. This section gives detailed information about framework and numerical scheme.

4.1. Framework

We considered a polydisperse powder flowing down an inclined plane. The angle of inclination is $\theta = 30^o$ with respect to the horizon and the powder is subjected to gravity. Fig. 2 reports a sketch of the system. The granular material is represented as a single solid phase, with bulk density equal to $\rho_s = 1260$ kg/m^3. This choice is motivated by the fact that the solid volume fraction is assumed uniform and constant within the powder bed. Even though all the particles are advected within the bulk flow, we could track the downward relative

motion between particles of different size thanks to the DQMOM transport equations (see Section 2.3).

4.2. Numerical scheme

To run the simulations, we used the commercial CFD code Ansys Fluent 17.2. As multifluid model, we employed the coupled level-set and volume of fluid method. The primary phase is ambient air whereas the secondary phase is the bulk solid. The two phases are immiscible, and mass transfer does not occur among them. The solid phase is composed of a polydisperse mixture of grains whose particle size distribution is approximated with a two-nodes quadrature formula. The quadrature weights and the quadrature weighted nodes were treated as user scalars, and their transport equations (Eqs. 15 and 16) were added to the default equations of the code. We also implemented the closure for the solid frictional viscosity (Eq. 38) by means of user defined functions.

We used the pressure-based solver, which is recommended for low-speed incompressible flows. To convert scalar transport equations into algebraic equations that are numerically solvable, the code adopts a finite-volume discretization scheme. For what concerns the spatial discretization, we used the Least Squares Cell-Based algorithm. We set a second order accurate level-set method, whereas momentum and user defined scalars were discretized through a first-order upwind scheme. Temporal discretization is first order accurate and implicit. To couple pressure and velocity, we adopted the SIMPLE (Simultaneous Solution of Non-linearly Coupled Equations) algorithm. We then adopted the compressive interface capturing scheme, which is particularly suitable for flows

with high ratios of viscosities between the phases. The pressure values at the cell-face are interpolated by a body-force-weighted scheme. To compute the flow variables, we used a maximum of 20 iterations for each time step. Setting the tolerance of all the variables equal to 10^{-3}, we usually attained convergence within the iteration limit. The time step was set to 10^{-3} s.

4.3. Boundary and initial conditions

The simulation domain is an inclined chute 1 m long and 3 cm high represented as a two-dimension computational grid. The effect of the front and back walls is therefore neglected. The mesh is uniform almost everywhere, with 15090 cells of 2 x 1 mm size (see Fig. 2). We assigned a no-slip boundary condition at the bottom wall (Hirshfeld and Rapaport, 1997; Silbert et al., 2003), and 100 Pa gauge pressure at the domain upper boundary and outlet boundary. With regard to the inflow, after several trial experiments, we saw that a good feed rate to induce a stable flow (Silbert et al., 2003) can be obtained by imposing a constant inlet velocity of 0.35 m/s for the solid phase.

In its initial state, the bulk solid is uniformly well-mixed and fill the chute height up to $H = 1.5$ cm. To assign the initial conditions, we need to know the values of the n quadrature weights and n quadrature nodes at time 0 and everywhere within the computational domain. For this purpose, we had first to calculate the first $2n$ order moments by implementing Eq. 17 to the volume density function of the particle size distribution (which is known). Since the quadrature approximation is Gaussian, the quadrature nodes and weights can be efficiently obtained from the moments of the density function by adopting

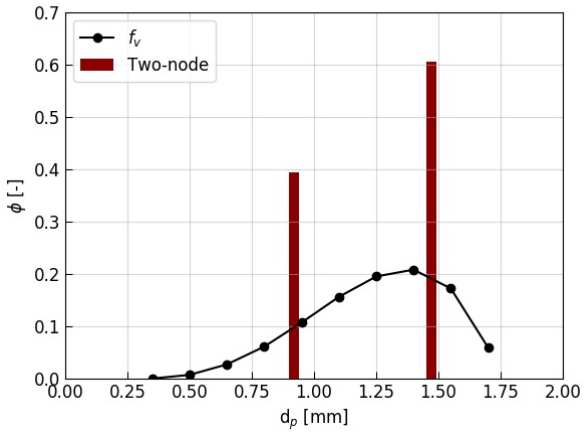

Figure 3: The simulated PSD expressed in terms of 10 different size classes and a two-node representation. The positions and the heights of the vertical lines represent the Dirac delta functions of the quadrature formula.

the product-difference algorithm of Gordon (McGraw, 1997). Fig. 3 shows the continuous particle size distribution of our granular system considering 10 different size classes (in reality the PSD is usually determined by sieve analysis and thus expressed in terms of discrete sizes), and its two-nodes representation. The values of its first four integer moments are reported, together with quadrature nodes and weights, in Tab. 1. Note that the zeroth order moment is equal to one since we are considering a void-free VDF. Finally, since the inflow is constant and uniform, we imposed constant fluxes of the user-defined scalars at the solid inlet.

Moments of the VDF			
$\mathcal{M}_0$ [-]	$\mathcal{M}_1$ [mm]	$\mathcal{M}_2$ [mm^2]	$\mathcal{M}_3$ [mm^3]
1	1.2535	1.6440	2.2346
Quadrature nodes and weights			
ξ_1 [mm]	ϕ_1 [-]	ξ_2 [mm]	ϕ_2 [-]
0.92	0.394	1.47	0.606

Table 1: Values of the VDF moments, quadrature nodes and weights obtained from the PSD reported in Fig. 3

5. DEM validation

The challenge is to validate the results of the CFD-PBE coupled model. A valuable tool to test and calibrate continuum models (Weinhart et al., 2013) when experimental observations are unfeasible (e.g. it is difficult to measure the evolving particle-size distribution of polydisperse systems during flow) is represented by Discrete Element Method (DEM) simulations. The 3D soft-sphere simulation was implemented in LIGGGHTS®-PUBLIC (Kloss et al., 2012), an open source DEM particle simulation software. As contact force model, we employed the non-linear spring-dashpot model developed by Hertz and Mindlin (Johnson and Jackson, 1987; Mindlin, 1949). This means that particles interact by elastic contact, whereas the normal dissipation is represented through a dashpot element. To account for gear-like rotation of two particles in contact, we used the constant directional torque (CDT) as rolling friction model.

Periodic boundary conditions are imposed in the stream-wise (x) and span-wise (y) directions. Periodic boundary conditions allow reducing the number of particles required, since only a sector of the full geometry is simulated. To

avoid plug flow, the bottom wall must be a rough surface. To model roughness, we fixed some particles to the base (Zheng and Hill, 1996).

The system is filled with a total of 3000 particles, all having the same intrinsic density ($\rho_s^* = 2000\text{kg/m}^3$). Unlike Marks et al. (2012), who simulated a polydisperse mixture of spheres distributed uniformly, we implemented a non-uniform particle size distribution (i.e. the 10 different size classes reported in Fig. 3). For all the particles, we defined the following material properties: Young's modulus, Poisson ratio, sliding friction coefficient, coefficient of restitution and coefficient of rolling friction. Since it has been shown that the use of a relatively small Young's modulus does not result in a significant error in structural analysis (Zhou et al., 2004), E was set of the order of magnitude of MPa instead of GPa. This reduces the computational time without significantly affecting flow patterns, velocity profiles and shear stresses (LIGGGHTS(R)-PUBLIC website, n.d.; Remy et al., 2009). The computational time step was set equal to 10^{-6} s, small enough to avoid the propagation of the disturbance farther than the immediate neighbourhood of each particle (Cundall and Strack, 1979). The simulation parameters are summarized in Tab. 2.

The simulation was initialized with gravitational acceleration acting in the negative z-direction (i.e. the plane is horizontal). The bed of particles was generated within the simulation domain and let settle by gravity. Once settled, the gravity vector was rotated to simulate the inclination angle θ. At that point, particles started to avalanche down-slope.

Variable	**Symbol**	**Value**
Particle density [kg/m^3]	ρ_s^*	2000
Young's modulus [MPa]	E	26
Poisson ratio	σ	0.25
Sliding friction coefficient	μ_s	0.56
Rolling friction coefficient	μ_r	0.001
Restitution coefficient	e_n	0.60
Number of particles	N_T	3000
Time step [s]	Δt	1e−6
Boundary conditions	−	p p f

Table 2: A summary of the DEM simulation parameters.

6. Results and discussion

As discussed above, the aim of this paper is to validate our segregation CFD-PBE coupled model. In this section, we report in order: the results from the CFD simulation, the results from the DEM simulation and the comparison between the two. In both cases, in order to evaluate segregation, we divided the domain, starting from the bottom, in three layers: a bottom layer, a top layer and a middle layer sandwiched in between. Each layer was 4 mm height in the z-direction.

6.1. CFD-PBE coupled model simulations

We ran the CFD simulation considering a two-node quadrature approximation for the PSD and constant mean values for drag coefficient and coefficient of diffusion. Following Marks et al. (2012), the diffusion coefficient had to be of the order of magnitude of $\mathscr{D} \sim 10^{-5}$ m^2/s. About the drag coefficient, suitable

values that lead to reasonable segregation velocities are about $c \sim 10^4 - 10^5$ s^{-2}. The results reported in this paper were obtained with $\mathscr{D} = 1.2 \cdot 10^{-5}$ m^{2}s^{-1} and $c = 6 \cdot 10^4$ s^{-2}. Furthermore, we set $\mu_s = 0.176$, $\mu_2 = 0.643$ and $I_0 = 0.279$, whereas the air was modelled with a density of 1.225 kg/m^3 and a viscosity of $1.7894 \cdot 10^{-5}$ Pa s. Then, we defined the investigation window at 0.8 ± 0.1m from the inlet (at the inlet the flux is constant and homogeneous).

The CFD simulations give the values of the quadrature weights and nodes in each computational cell of the domain; from these values we can obtain the cell values of the first four integer moments. Thus, we just have to divide the bed in layers and from the numerical profiles of the VDF moments determine their average values in each layer and then the corresponding average values of the quadrature nodes and weights. Fig. 4 shows the evolution in time of the first raw moment, which represents the mean particle diameter. We can distinguish three inversely graded segregated layers characterized by finer particles at the bottom, coarser grains on top, and medium-sized particles in between. This means that, as expected, smaller particles have, on average, a net downward motion, thus particles segregate by size. Segregation is even more pronounced at the bottom, where the shear rate is higher.

The evolution of the two nodes, still for the three layers, is shown in Fig. 5. More CFD-PBE results are reported in the Supplementary Information.

6.2. DEM simulation

The DEM simulation treats a section 2 cm long and 1 cm wide of the full geometry considered in the CFD simulation; this is because simulating the entire

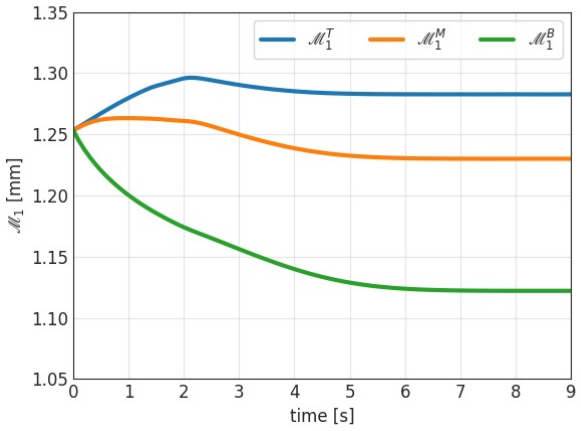

Figure 4: Evolution of the first order moment of the PSD in the bottom, middle and top layers obtained by solving the CFD-PBE coupled model.

geometry would require more than $1.5 \cdot 10^5$ particles.

Fig. 6 displays three snapshots of the simulation, where the different colours denote different sized particles. At time $t = 0$ s particles are homogeneously distributed, whereas at time $t = 6$ s the system has already reached its final steady state.

Unlike continuum models, the results of DEM simulations yield the position of each particle at any given time. This allowed us to determine the numerical fraction of each size class in each layer, to reconstruct the PSD in terms of volume density function (see. Fig. 7), and to calculate the first four moments of the distribution. The smaller particles collect preferentially close to the bottom, whereas the top is richer in bigger particles. From the VDF moments, we back-calculated the two weights and two nodes of the distribution by employing the product-difference algorithm of Gordon (Gordon, 1968). These are used in the

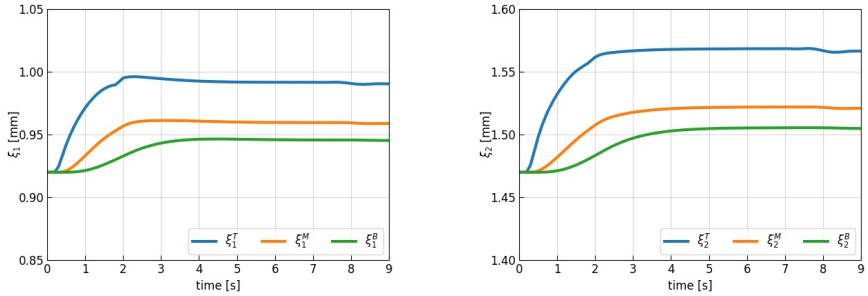

Figure 5: Evolution of the first (on the left) and second (on the right) quadrature node in the bottom, middle and top layer obtained by solving the CFD-PBE coupled model.

following section for model validation.

6.3. Confirming the model

First, we wanted to verify that the velocity field is correctly predicted by the rheological model. We therefore performed preliminary simulations both in CFD and DEM considering a monodisperse bed of particles, all having diameter equal to the mean particle diameter of the distribution reported in Fig. 3 (= 1.25 mm). Fig. 8 shows the streamwise velocity profile (i.e. the x component of the velocity vector as a function of the z coordinate) of the mono-sized bed of grains at steady state in the two cases. The velocity profiles agree, with a R-squared value of 0.994. Thus the shear rate profile, which induces segregation, must be similar, and the two granular flows comparable.

Fig. 9 reports the evolution of quadrature weights (first column) and weighted nodes (second column) obtained from both our CFD-PBE coupled model (coloured lines) and DEM simulations (black lines). The results refer to the top, middle and bottom layers and show that segregation is less pronounced on top,

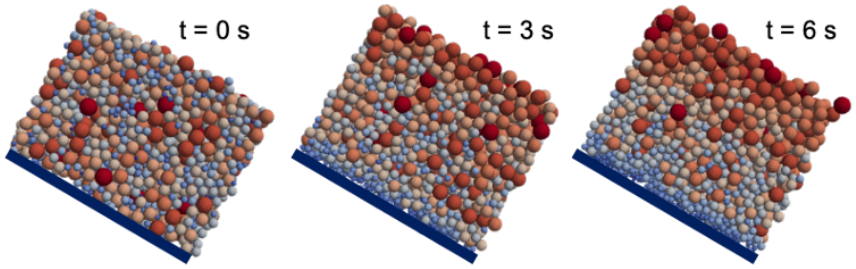

Figure 6: Snapshots from the DEM simulation. The system is filled with 3000 particles characterized by the volume density PSD reported in Fig. 3. The colors denote the particle diameter. At $t = 0$ s, the sample is well mixed. At time $t = 6$ s, the system has reached steady state and the segregation profile has fully developed.

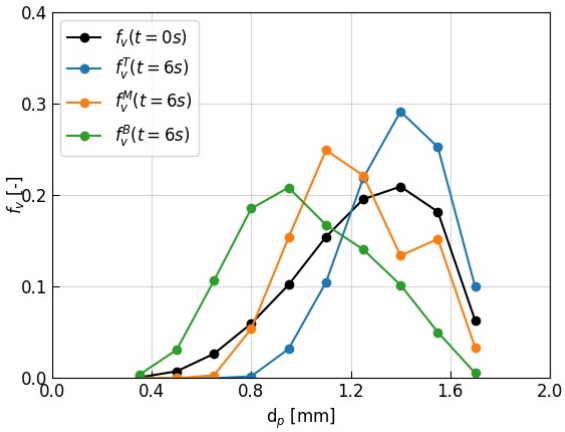

Figure 7: Particle size distribution at $t = 0$ s (black line), and after 6 s (coloured lines) in the three layers from DEM simulations.

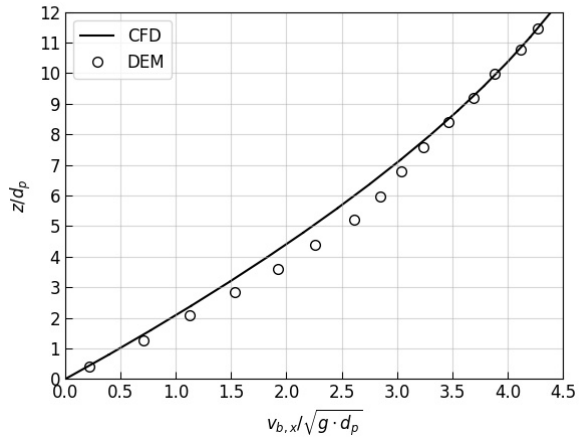

Figure 8: Comparison of the dimensionless streamwise velocity profile as a function of z/d_p obtained with DEM and CFD simulations.

where the shear rate is smaller, and increases as the bottom wall is approached. The CFD-PBE coupled model predicts well the evolution of both weights and weighted nodes in the middle and top layers, but not in the bottom layer. This disagreement will be discussed in the following section.

Figs. 10, 11 and 12 report the PSDs and their two-node quadrature representations achieved after 6 s in the bottom, middle and top layers, respectively. The vertical lines, whose positions and heights are the quadrature nodes and quadrature weights, represent the Dirac delta functions of the quadrature formulas. As we can see, the results of the CFD-PBE and DEM simulations agree very well in the middle layer, and quite well in the top layer. However, the results differ in the bottom layer. There, the positions indicate the quadrature nodes are over-estimated. Moreover, if the weight of the first node is overestimated, the weight of the second node is underestimated.

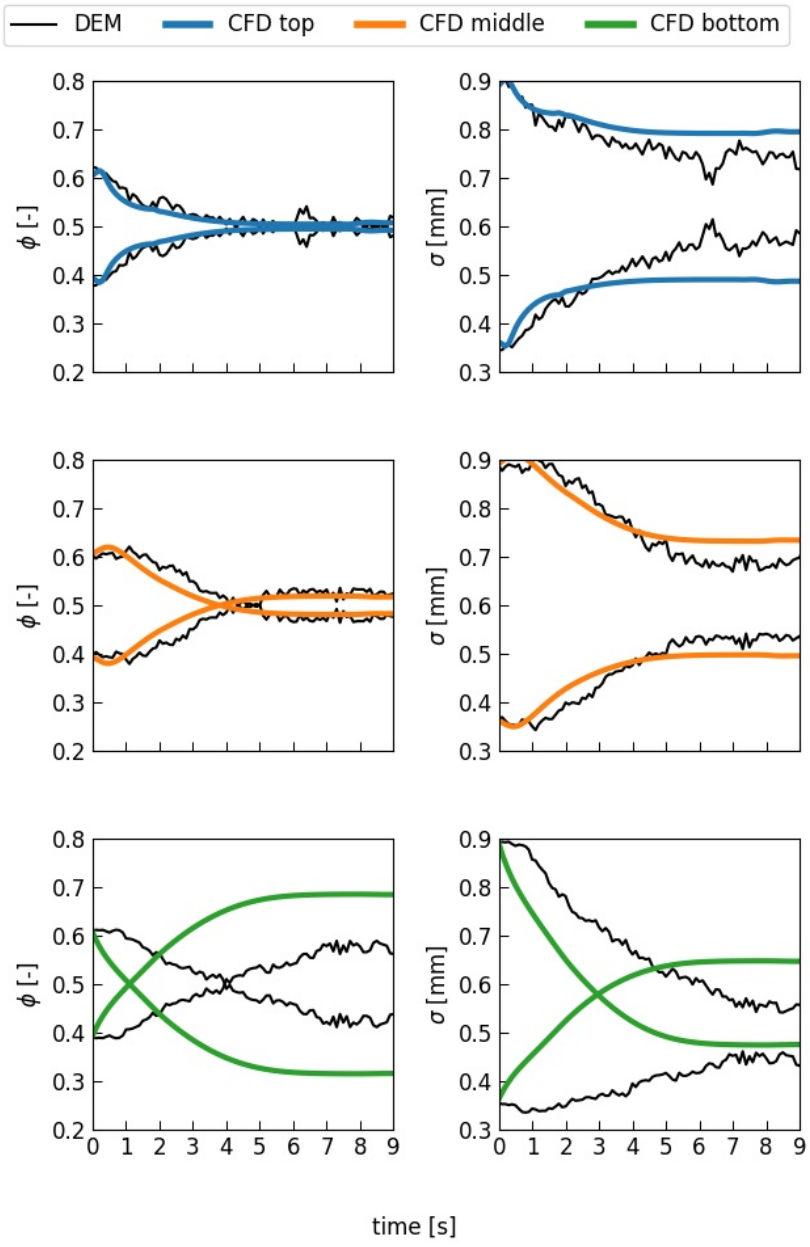

Figure 9: Evolution of the quadrature weights (on the left) and weighted nodes (on the right) obtained from the segregation CFD-PBE coupled model (coloured lines) and the DEM simulation (black line). The results refer to the top, middle and bottom layers.

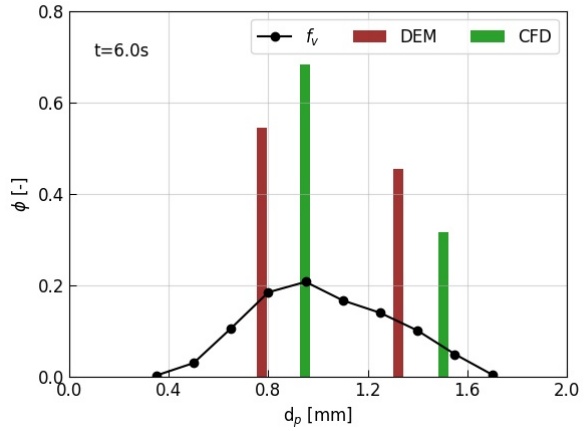

Figure 10: PSD at the bottom of the chute after $t = 6$ s. The red lines represent the two-node representation obtained from the DEM simulation, while the green lines are the two-node representation obtained from the CFD simulation.

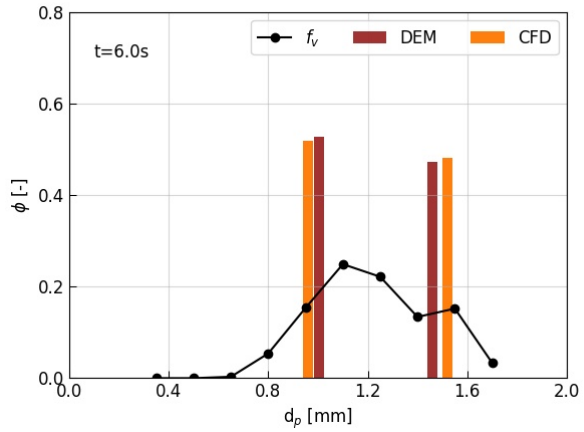

Figure 11: PSD in the middle layer at $t = 6$ s. The red lines represent the two-node representation obtained from the DEM simulation, while the orange lines are the two-node representation obtained from the CFD simulation.

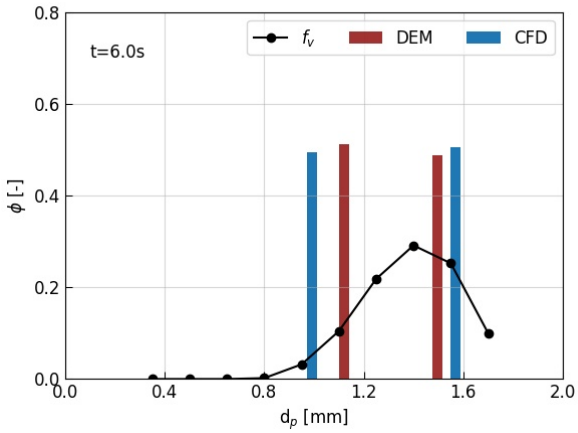

Figure 12: PSD in the top layer at $t = 6$ s. The red lines represent the two-node representation obtained from the DEM simulation, while the blue lines are the two-node representation obtained from the CFD simulation.

Thus, despite our CFD-PBE coupled model works for a range of conditions, it fails under some circumstances. The limitations of our model are not directly related to the CFD-PBE framework but rather to the assumptions we made of constant and isotropic diffusion, constant drag coefficient, and uniform and constant bed porosity.

6.4. Discussion

We can justify the observed discrepancies on theoretical grounds by examining the assumptions we employed in the CFD-PBE model regarding diffusion, drag coefficient and bed porosity.

In granular flows, diffusion has mainly been studied for monodisperse particle systems. According to Utter and Behringer (2004), who studied the random

motion of monodisperse grains in a two-dimensional Couette shearing experiment, the self-diffusivity is proportional to the local shear rate and to the square of the particle radius (i.e. $\mathscr{D} \propto \dot{\gamma} d^2$). In chute flows of bidisperse disks, Berton et al. (2003) observed that the diffusive process is independent of the particle size and that the diffusion coefficient associated with each layer increases linearly with the layer height. Since the shear rate decreases when the height increases, being maximum at the wall, it follows that $\mathscr{D}$ should not depend on the particle size and should decrease with the shear rate. This disagrees with what Utter and Behringer (2004) reported. More recently, Chassagne et al. (2020) showed that the diffusion coefficient should depend on the inertial number.

The articles just cited reveal that the process of particle diffusion in dense monodisperse granular media is still unclear and reliable constitutive equations are unavailable. For dense polydisperse granular media, this is all the more true (Chassagne et al., 2020). This is why we decided to model the process as isotropic using a constant coefficient of diffusion. To better address the problem of inhomogeneous diffusion coefficients, one could carry out simulations based on a classical random walk (Berton et al., 2003), but this is beyond the scope of this paper.

In this work, we further assumed a linear drag law with constant drag coefficient c, even though c is expected to be a function of the Reynolds number (Re), Froude number (Fr), particle concentration, particle size, restitution coefficient and flow depth (Gauer et al., 2007; Panaitescu et al., 2017). The absence of constitutive equations accounting for these dependences (Marks et al., 2012)

justifies our modeling choice.

Finally, even if it is well-known that the packing porosity varies with the size distribution of the materials involved (Ouchiyama and Tanaka, 1986), we neglected this effect. Accounting for variations in the local porosity would require a more expensive multiphase model than the coupled level-set and volume of fluid (VOF) method.

To prove that the inconsistency of the results is due to the assumptions we made and not to the CFD-PBE coupling framework, we have reported in Fig. 13 the evolution of weights and weighted nodes obtained at the bottom layer for different values of the parameters $\mathscr{D}$ and a constant value of the drag coefficient (i.e. $c = 6 \cdot 10^4$ s^{-1}). As expected, the higher the diffusion coefficient, the lower the degree of segregation. Analogously, Fig. 14 reports the evolution of weights and weighted nodes obtained at the bottom layer for different values of the drag coefficient and same diffusion (i.e. $\mathscr{D} = 1.2 \cdot 10^{-5}$m^{2}s^{-1}). At increasing values of the drag coefficient, the segregation process becomes slower and less pronounced. Thus, to quantitatively change the results in the bottom layer, one should al least define drag and diffusion coefficients as functions of the bed depth.

All these considerations suggest that the main features of the CFD-PBE model are correct; the evolution of weights and weighted nodes is well predicted for a high portion of the flow depth. Nevertheless, to improve the accuracy of the model, in particular in the region close to the wall, we must describe the gravity-induced segregation process and the shear-induced diffusion process

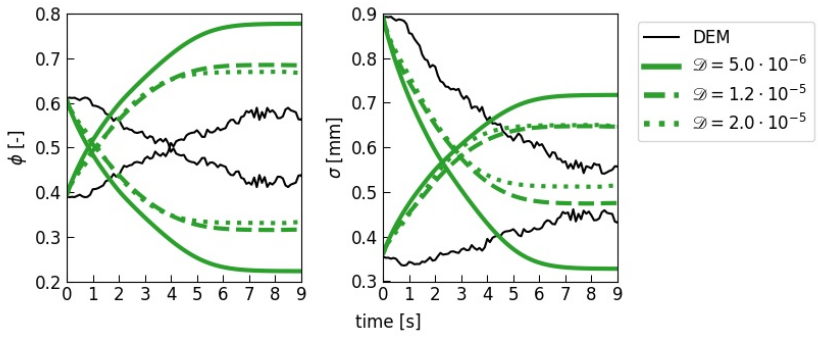

Figure 13: Evolution of weights (on the left) and weighted nodes (on the right) in the bottom layer obtained with constant drag ($c = 6 \cdot 10^4 \mathrm{s}^{-1}$) and different values of the parameters $\mathscr{D}$ using the CFD-PBE coupled model. The solid black lines represent the DEM results and are reported for comparison.

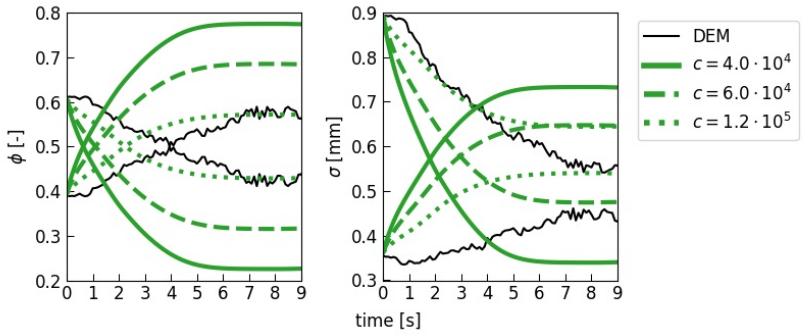

Figure 14: Evolution of weights (on the left) and weighted nodes (on the right) in the bottom layer obtained with different values of the drag coefficient and same diffusivity ($\mathscr{D} = 10^{-5} \mathrm{m}^2 \mathrm{s}^{-1}$) using the CFD-PBE coupled model. The solid black lines represent the DEM results and are reported for comparison.

more accurately. This requires more physical insight into these processes and more reliable constitutive equations.

7. Conclusion

In this paper, we presented a new CFD-PBE coupled model for describing segregation in dense polydisperse granular flows. The PBE was solved with the direct quadrature method of moments proposed by Marchisio and Fox (2005). We adopted a two-node quadrature approximation of the particle size distribution and used a segregation-remixing model to close the size-conditioned particle velocity. The $2n$ resulting transport equations were then implemented in Ansys fluent. To track the interface between the granular medium and air, we used the coupled level-set and VOF method. To determine the velocity field in the granular mixture, we employed the rheological model of Jop et al. (2006). To test the model, we modelled segregation in a granular mixture with an arbitrary polydisperse grain size distribution flowing down an inclined plane and we compared the results to those of DEM simulations. This geometry was chosen for its importance and simplicity but our results should be broadly applicable to other dense granular flows.

The CFD-PBE coupled model predicts reasonably well the segregation process. It has a considerable benefit and, unlike DEM, allows simulating large polydisperse powder systems with reasonable computational cost. This is a relevant step forward for the scale-up and design of all those industrial applications that employ granular materials in large quantities as it happens, for instance,

in agriculture, chemical engineering industries and mining.

Despite its advantages, the model has a few drawbacks. It requires constitutive equations for the gravity-induced segregation process and the shear-induced diffusion process, processes that strongly influence the numerical results. Even though in the literature there are a lot of studies, the constitutive equations for these processes are still unreliable and inaccurate, often controversial, and many fundamental questions still remain to be answered.

Acknowledgements

With the support of the Erasmus+ for Traineeships programme of the European Union.

References

Alonso, M., Satoh, M., Miyanami, K., 1991. Optimum combination of size ratio, density ratio and concentration to minimize free surface segregation. Powder Technology 68 (2), 145–152.

Arastoopour, H., Gidaspow, D., Abbasi, E., 2017. Computational Transport Phenomena of Fluid-Particle Systems. Springer.

Barker, T., Gray, J. M., 2017. Partial regularisation of the incompressible μ(I)-rheology for granular flow. Journal of Fluid Mechanics 828, 5–32.

Berton, G., Delannay, R., Richard, P., Taberlet, N., Valance, A., 2003. Two-dimensional inclined chute flows: Transverse motion and segregation. Physical Review E 68 (5), 51303.

Bhattacharya, T., McCarthy, J. J., 2014. Chute flow as a means of segregation characterization. Powder Technology 256, 126–139.

Bridgwater, J., 1976. Fundamental powder mixing mechanisms. Powder Technology 15 (2), 215–236.

Bridgwater, J., 1994. Mixing and segregation mechanisms in particle flow. In: Granular matter. Springer, pp. 161–193.

Chassagne, R., Maurin, R., Chauchat, J., Gray, J., Frey, P., 2020. Discrete and continuum modelling of grain size segregation during bedload transport. Journal of Fluid Mechanics 895.

Cundall, P. A., Strack, O. D., 1979. A discrete numerical model for granular assemblies. Geotechnique 29 (1), 47–65.

Da Cruz, F., Emam, S., Prochnow, M., Roux, J. N., Chevoir, F., 2005. Rheophysics of dense granular materials: Discrete simulation of plane shear flows. Physical Review E 72 (2).

Dianat, M., Skarysz, M., Garmory, A., 2017. A Coupled Level Set and Volume of Fluid method for automotive exterior water management applications. International Journal of Multiphase Flow 91, 19–38.

Fan, Y., Jacob, K. V., Freireich, B. J., Lueptow, R. M., 2017. Segregation of granular materials in bounded heap flow: A review. Powder Technology 312, 67–88.

G. D. R. MiDi, 2004. On dense granular flows. European Physical Journal E 14 (4), 341–365.

Gauer, P., Issler, D., Lied, K., Kristensen, K., Iwe, H., Lied, E., Rammer, L., Schreiber, H., 2007. On full-scale avalanche measurements at the ryggfonn test site, norway. Cold Regions Science and Technology 49 (1), 39–53.

Gordon, R. G., 1968. Error bounds in equilibrium statistical mechanics. Journal of Mathematical Physics 9 (5), 655–663.

Gray, J. M., 2018. Particle Segregation in Dense Granular Flows. Annu. Rev. Fluid Mech 50 (1), 407–33.

Gray, J. M., Ancey, C., 2011. Multi-component particle-size segregation in shallow granular avalanches. Journal of Fluid Mechanics 678, 535–588.

Gray, J. M., Thornton, A. R., 2005. A theory for particle size segregation in shallow granular free-surface flows. Proceedings of the Royal Society A: Mathematical, Physical and Engineering Sciences 461 (2057), 1447–1473.

Gray, J. M. N. T., Chugunov, V. A., 2006. Particle-size segregation and diffusive remixing in shallow granular avalanches. Journal of Fluid Mechanics 569, 365–398.

Heyman, J., Delannay, R., Tabuteau, H., Valance, A., 2017. Compressibility regularizes the μ(I)-rheology for dense granular flows. Journal of Fluid Mechanics 830, 553–568.

Hirshfeld, D., Rapaport, D. C., 1997. Molecular dynamics studies of grain segregation in sheared flow. Physical Review E 56 (2), 2012–2018.

Johnson, C. G., Jackson, R., 1987. Frictional-collisional constitutive relations for granular materials, with application to plane shearing. Journal of Fluid Mechanics 176, 67–93.

Jop, P., Forterre, Y., Pouliquen, O., 2006. A constitutive law for dense granular flows. Nature 441 (7094), 727–730.

Kloss, C., Goniva, C., Hager, A., Amberger, S., Pirker, S., 2012. Models, algorithms and validation for opensource dem and cfd–dem. Progress in Computational Fluid Dynamics, an International Journal 12 (2-3), 140–152.

LIGGGHTS(R)-PUBLIC website, n.d. https://www.cfdem.com.

Marchisio, D. L., Fox, R. O., 2005. Solution of population balance equations using the direct quadrature method of moments. Journal of Aerosol Science 36 (1), 43–73.

Marchisio, D. L., Fox, R. O., 2007. Multiphase reacting flows: modelling and simulation. Springer.

Marchisio, D. L., Fox, R. O., 2013. Computational models for polydisperse particulate and multiphase systems. Cambridge University Press.

Marchisio, D. L., Pikturna, J. T., Fox, R. O., Vigil, R. D., Barresi, A. A., 2003a. Quadrature method of moments for population-balance equations. AIChE Journal 49 (5), 1266–1276.

Marchisio, D. L., Vigil, R. D., Fox, R. O., 2003b. Quadrature method of moments for aggregation-breakage processes. Journal of Colloid and Interface Science 258 (2), 322–334.

Marks, B., Rognon, P. G., Einav, I., 2012. Grainsize dynamics of polydisperse granular segregation down inclined planes. Journal of Fluid Mechanics 690, 499–511.

Mazzei, L., 2011. Limitations of quadrature-based moment methods for modeling inhomogeneous polydisperse fluidized powders. Chemical Engineering Science 66 (16), 3628–3640.

Mazzei, L., 2013. Segregation dynamics of dense polydisperse fluidized suspensions modeled using a novel formulation of the direct quadrature method of moments. Chemical Engineering Science 101, 565–576.

Mazzei, L., Marchisio, D. L., Lettieri, P., 2010. Direct quadrature method of moments for the mixing of inert polydisperse fluidized powders and the role of numerical diffusion. Industrial and Engineering Chemistry Research 49 (11), 5141–5152.

Mazzei, L., Marchisio, D. L., Lettieri, P., 2012. New Quadrature-Based Moment Method for the Mixing of Inert Polydisperse Fluidized Powders in Commercial CFD Codes. AIChE Journal 58 (10), 3054–3069.

McCarthy, J. J., 2009. Turning the corner in segregation. Powder Technology 192 (2), 137–142.

McGraw, R., 1997. Description of aerosol dynamics by the quadrature method of moments. Aerosol Science and Technology 27 (2), 255–265.

Mindlin, R. D., 1949. Compliance of elastic bodies in contact. Journal of Applied Mechanics 16, 259–268.

Olsson, E., Kreiss, G., Zahedi, S., 2007. A conservative level set method for two phase flow II. Journal of Computational Physics 225 (1), 785–807.

Ottino, J. M., Khakhar, D. V., 2000. Mixing and segregation of granular materials. Annual review of fluid mechanics 32 (1), 55–91.

Ouchiyama, N., Tanaka, T., 1986. Porosity estimation from particle size distribution. Industrial and Engineering Chemistry Fundamentals 25 (1), 125–129.

Panaitescu, A., Clotet, X., Kudrolli, A., 2017. Drag law for an intruder in granular sediments. Physical Review E 95 (3), 1–7.

Pitman, E. B., Schaeffer, D. G., 1987. Stability of time dependent compressible granular flow in two dimensions. Communications on Pure and Applied Mathematics 40 (4), 421–447.

Ramkrishna, D., 2000. Population Balances: Theory and Applications to Particulate Systems in Engineering. Elsevier.

Remy, B., Khinast, J. G., Glasser, B. J., 2009. Discrete element simulation of free flowing grains in a four-bladed mixer. AIChE Journal 55 (8), 2035–2048.

Rognon, P. G., Roux, J. N., Naaïm, M., Chevoir, F., 2007. Dense flows of bidisperse assemblies of disks down an inclined plane. Physics of Fluids 19 (5), 15–19.

Savage, S. B., Lun, C. K., 1988. Particle size segregation in inclined chute flow of dry cohesionless granular solids. Journal of Fluid Mechanics 189, 311–335.

Schaeffer, D. G., Barker, T., Tsuji, D., Gremaud, P., Shearer, M., Gray, J. M., 2019. Constitutive relations for compressible granular flow in the inertial regime. Journal of Fluid Mechanics 874, 926–951.

Silbert, L. E., Landry, J. W., Grest, G. S., 2003. Granular flow down a rough

inclined plane: Transition between thin and thick piles. Physics of Fluids 15 (1), 1–10.

Standish, N., 1985. Studies of size segregation in filling and emptying a hopper. Powder Technology 45 (1), 43–56.

Strumendo, M., Arastoopour, H., 2008. Solution of PBE by MOM in finite size domains. Chemical Engineering Science 63 (10), 2624–2640.

Tripathi, A., Khakhar, D. V., 2011. Rheology of binary granular mixtures in the dense flow regime. Physics of Fluids 23 (11).

Tunuguntla, D. R., Bokhove, O., Thornton, A. R., 2014. A mixture theory for size and density segregation in shallow granular free-surface flows. Journal of Fluid Mechanics 749, 99–112.

Umbanhowar, P. B., Lueptow, R. M., Ottino, J. M., 2019. Modeling segregation in granular flows. Annual Review of Chemical and Biomolecular Engineering 10, 129–153.

Utter, B., Behringer, R. P., 2004. Self-diffusion in dense granular shear flows. Physical Review E 69 (3), 1–12.

Volpato, S., Tirapelle, M., Santomaso, A. C., 2020. Modeling and experimental investigation of shear-induced particle percolation in diluted binary mixtures. Physical Review E 102 (1), 1–8.

Weinhart, T., Luding, S., Thornton, A. R., 2013. From discrete particles to

continuum fields in mixtures. AIP Conference Proceedings 1542 (1), 1202–1205.

Yohannes, B., Hill, K. M., 2010. Rheology of dense granular mixtures: Particle-size distributions, boundary conditions, and collisional time scales. Physical Review E 82 (6), 1–9.

Zheng, X. M., Hill, J. M., 1996. Molecular dynamics modelling of granular chute flow: Density and velocity profiles. Powder Technology 86 (2), 219–227.

Zhou, F., Advani, S. G., Wetzel, E. D., 2004. Slow drag in granular materials under high pressure. Physical Review E 69 (6), 7.